Underestimates of Orographic Precipitation in Idealized Simulations. Part II: Underlying Causes

LYDIA TIERNEY[a] AND DALE DURRAN[a]

[a] *University of Washington, Seattle, Washington*

(Manuscript received 27 September 2023, in final form 15 May 2024, accepted 3 June 2024)

ABSTRACT: Warm-sector orographic precipitation in a midlatitude cyclone encountering a ridge is simulated in a "Cyc+Mtn" experiment. A second "Shear" simulation is conducted with horizontally uniform unidirectional flow over the same mountain having thermodynamic and cross-mountain wind profiles identical to those on the centerline in the "Cyc+Mtn" simulation. The relationship between integrated vapor transport (IVT) and orographic precipitation in the Mtn+Cyc case is consistent with observations, yet the same IVT in the Shear simulation produces far less precipitation. The difference between the precipitation rates in the Cyc+Mtn and Shear cases is traced to differences in the cross-mountain moisture-flux convergence and is further isolated to differences in the cross-mountain-velocity convergence over the windward slope. The winds at the ridge crest are stronger in the Shear case, leading to more velocity divergence and decreased moisture-flux convergence. The stronger ridge-crest winds in the Shear case are produced by a stronger mountain wave, which persists after being generated during the artificial startup of the Shear simulation. Initializing with a gradually ramped-up unidirectional flow and integrating to a quasi-steady state fails to adequately capture the processes regulating the leeside circulations. Even worse results are obtained if the shear flow is instantaneously accelerated from rest. An alternative microphysical explanation for the precipitation difference between the Cyc+Mtn and Shear simulations is examined using additional numerical experiments that enhance the seeder–feeder process. Although such enhancements increase precipitation, the increase is too small to account for the differences between the Cyc+Mtn and Shear simulations.

SIGNIFICANCE STATEMENT: Our results highlight the difficulty in conducting studies of mesoscale atmospheric circulations in isolation from their surrounding environment. This approach often allows for more computationally efficient and detailed analysis of the target phenomena by reducing the size of the computational domain. But, at least in the case of orographic precipitation, such isolation can significantly limit the realism of the simulated process.

KEYWORDS: Mountain waves; Precipitation; Cloud microphysics; Orographic effects; Mesoscale models; Model evaluation/performance

1. Introduction

The precipitation generated by midlatitude cyclones is enhanced when they encounter orography. In landfalling cyclones, a large fraction of such orographically enhanced precipitation falls during the passage of the warm sector, when preexisting rainbands and frontal circulations are not present and the vertical profile of the upstream environmental winds is approximately unidirectional (Zagrodnik et al. 2019). Streams of enhanced horizontal water-vapor flux, known as atmospheric rivers, are often present in the warm sector, and there is a strong correlation between the upslope water-vapor flux and precipitation over the windward mountain slopes (Neiman et al. 2009; Kingsmill et al. 2016).

In Part I of this study, Tierney and Durran (2024, hereafter LT1) show that there is a similar strong correlation between the integrated upslope vapor transport ($IVT_{\perp}$) and the precipitation observed over a network of rain gauges deployed in the Olympic Mountains of western Washington during the 2015–16 Olympic Mountains Experiment (OLYMPEX) campaign (Houze et al. 2017). Furthermore, the correlations between integrated water-vapor transport and precipitation over the Olympic Mountains and those obtained from observations in the coastal mountains of Northern California by Kingsmill et al. (2016) are almost identical. LT1 also examine the relation between $IVT_{\perp}$ and precipitation in six idealized process studies in which orographic precipitation was forced by unidirectional horizontal upstream flows, and unsurprisingly, the two quantities are again highly correlated. But unexpectedly, the increase in the orographic precipitation rate as a function of integrated vapor transport (IVT) in the observed events is more than twice as large as that in the idealized studies, for both moist airflow over simple mountain shapes (Colle 2004; Cannon et al. 2012; Siler and Durran 2015; Kirshbaum and Schultz 2018) and those specifically targeting the Olympic Mountains and using the actual orography (Picard and Mass 2017; Purnell and Kirshbaum 2018). Moreover, Picard and Mass (2017) and Purnell and Kirshbaum (2018) conducted simulations using the Weather Research and Forecasting (WRF) Model, whose precursor, the Fifth-generation Pennsylvania State University–National Center for Atmospheric Research Mesoscale Model (MM5), accurately simulated total rainfall for the full rainy season and for the sum of the largest events for several years over the same area sampled during OLYMPEX (Minder et al. 2008).

Corresponding author: Dale Durran, drdee@uw.edu

DOI: 10.1175/JAS-D-23-0176.1

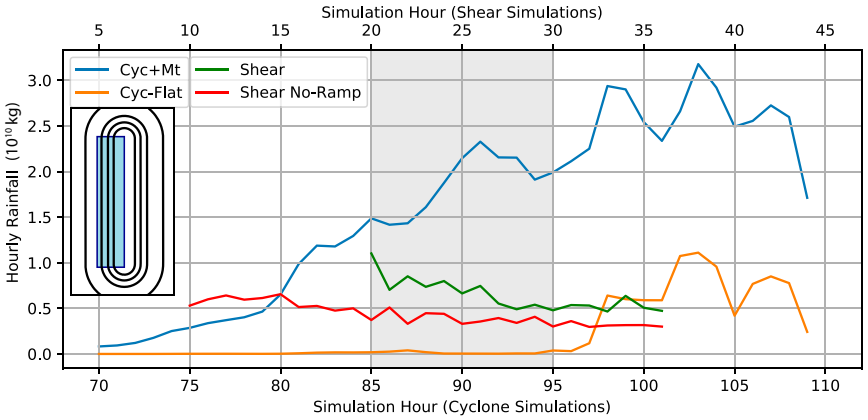

FIG. 1. The mean hourly precipitation integrated over the region containing the windward slope of the ridge (blue shaded area in the inset) plotted as a function of simulation time: Cyc+Mtn case (blue), Cyc-Flat case (orange), Shear case (green; plot begins at the end of the 20-h ramp-up), and Shear-No-Ramp case (red). The 10-h period used for the majority of our comparisons is shaded gray.

To better explore the source of this discrepancy between observations and process-study simulations, LT1 conducted idealized simulations that included both the synoptic-scale system and fine-scale orographic forcing. Using the WRF Model, they simulated a midlatitude cyclone in an *f*-plane channel encountering an isolated north–south ridge. The IVT–precipitation relationship over the central section of the ridge in this Cyc+Mtn simulation matches that for the observed events. They also performed a "Shear" simulation forced by a unidirectional environmental flow with thermodynamic and cross-mountain wind speed profiles representative of those at a location upstream of the ridge in the Cyc+Mtn environment.[1] By construction, the IVT in the Shear simulation was matched to that in the Cyc+Mtn case, but the precipitation rate was much lower in the Shear simulation. Instead, the IVT–precipitation relationship in the Shear simulation was characteristic of that in previously published process studies driven by unidirectional upstream flows.

In the following, we analyze the factors responsible for the difference between the precipitation rates in the Cyc+Mtn and the Shear simulations. We hypothesize these are the same factors responsible for the differences in the IVT–precipitation relations between the observed events and the idealized process studies of orographic precipitation documented in LT1. We will investigate the possible differences in both dynamical and microphysical processes. In section 2, we review the key properties of the three simulations we conducted in LT1. In section 3, we investigate the dynamical processes responsible for this difference by analyzing the differences in moisture-flux convergence over the windward slope of the mountain. In section 4, we consider the possibility that the differences in the precipitation rate are produced by synoptic-scale ascent generating falling ice crystals that subsequently enhance the rainfall via the seeder–feeder mechanism (Bergeron 1965). Section 5 contains the conclusions.

2. Precipitation in the Cyc-Flat, Cyc+Mt, Shear, and Shear No-Ramp simulations

The configuration of our three basic idealized numerical experiments was presented in LT1, along with a comparison of the precipitation totals. To recap, the windward-slope precipitation, integrated between $x = 800$ km and the crest at $x = 900$ km, is plotted as a function of simulation time for the Cyc+Mt, Cyc-Flat, and Shear cases in Fig. 1. In the Cyc+Mt case, orographic precipitation starts at 70 h, well before the warm front encounters the mountain. After the warm front passes, at about hour 81, the precipitation jumps up and then gradually increases during the warm-sector period. Finally, there is another upward jump in the precipitation as the cold front arrives at the northern end of the ridge near hour 97. In contrast, in the Cyc-Flat case, there is almost no precipitation in the spatial location of the virtual ridge until the passage of the cold front.

Despite being initialized with a horizontally uniform sounding from the warm-sector period in the Cyc-Flat simulation at 96 h just upstream of the position of the virtual ridge, the precipitation in the Shear case is much lighter than that in the Cyc+Mtn case. Also plotted for future reference is the precipitation produced in the Shear-No-Ramp simulation, which is identical to the Shear simulation except the environmental cross-mountain winds are not gradually ramped up from zero over a 20-h period but simply initialized at full strength. The Shear simulation, which attempts to mimic the gradual acceleration of the low-level cross-mountain winds as the cyclone approaches the ridge in the Cyc+Mt case, clearly produces more precipitation than the Shear-No-Ramp case. The cause of the differences in precipitation in the two shear-flow cases will be discussed in section 3c.

[1] To avoid any upstream influence from the ridge, the sounding was actually taken from the same point in our Cyc-Flat simulation, which is identical to the Cyc+Mtn simulation except that the terrain is flat.

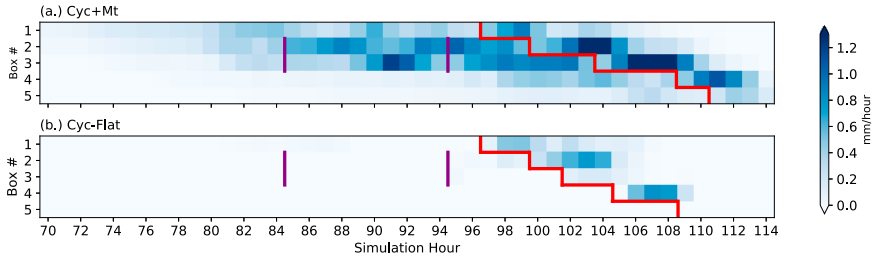

FIG. 2. Hourly and spatially averaged precipitation rates (mm h^{-1}) in each of five boxes equally dividing the blue shaded upslope region in Fig. 1 in a north-to-south direction: (a) Mtn+Cyc case and (b) Cyc-Flat simulation. Purple vertical lines drawn for boxes 2 and 3 delimit the 10-h warm-sector period beginning at 85 and ending at 95 h. (Tick marks are centered on each hour.) Red line segments mark the approximate arrival of the cold front precipitation in each box.

The evolving north–south distribution of the windward-slope precipitation is summarized in Fig. 2, in which the color fill indicates the hourly precipitation rate averaged over each of five 100 km × 100 km boxes spanning the windward slope of the ridge (shaded blue in the inset in Fig. 1). Numbering these boxes 1–5 from north to south, the precipitation rate within each box is plotted as a function of time. The north to south progression of the leading edge of the cold frontal precipitation is indicated by the red line segments in both the Mtn+Cyc and Cyc-Flat cases and is just slightly different between these cases. It is again evident that there is essentially no warm-sector precipitation falling in the Cyc-Flat case, whereas there is abundant warm-sector precipitation in the Mtn+Cyc case, and it is clearly heaviest in boxes 2 and 3. The dominant contributions from this section of the ridge are also evident in Fig. 3, which plots hourly rainfall in the Mtn+Cyc case as a function of time, area integrated over box 1, boxes 2 and 3, and boxes 4 and 5. The precipitation over boxes 2 and 3 during the 10-h period from 85 to 95 h will be the focus of much of the subsequent analysis.

3. Moisture-flux convergence and precipitation

The differences in precipitation in the Mtn+Cyc, Cyc-Flat, and Shear simulations are reflected in differences in the moisture budget over the windward slopes of the orography (or the virtual mountain in the same spatial location in the Cyc-Flat case).

a. *The moisture budget*

Neglecting diffusive mixing, the total-water mixing ratio q satisfies

$$\frac{\partial \rho q}{\partial t} + \nabla \cdot \rho q \mathbf{v} + \frac{\partial \rho q_r V_r}{\partial z} + \frac{\partial \rho q_s V_s}{\partial z} + \frac{\partial \rho q_g V_g}{\partial z} = 0, \qquad (1)$$

where ρ is the density of dry air, $\mathbf{v}$ is the 3D velocity vector, the mixing ratios of the falling microphysical species, rain, snow, and graupel are q_r, q_s, and q_g, and their fall velocities are V_r, V_s, and V_g, respectively. Integrating from the surface to the top of the domain, and letting $\overline{()}^s$ denote integration over the domain with respect to coordinate s, (1) reduces to

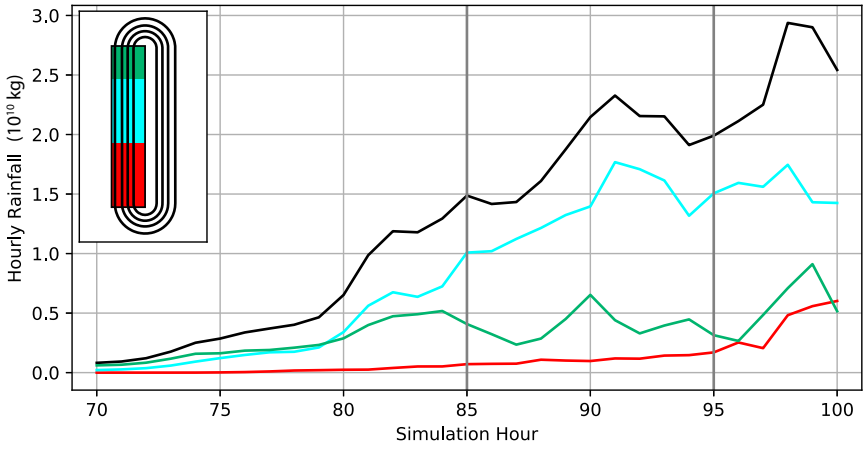

FIG. 3. Hourly precipitation in the Mtn+Cyc case as a function of time integrated over each of the three regions on the upslope side of the ridge indicated in the subplot: box 1 (green), boxes 2 and 3 (cyan), and boxes 4 and 5 (red). Black curve shows the total precipitation over all three regions.

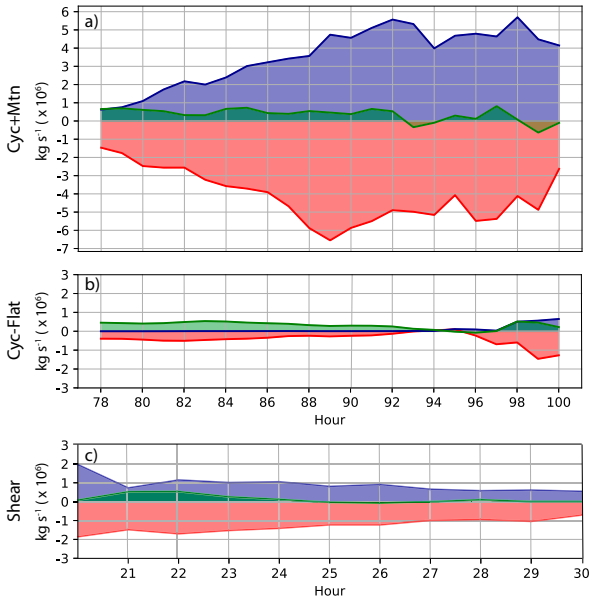

FIG. 4. Volume-integrated moisture budget over boxes 2 and 3 plotted as a function of time over 78–100 h for the (a) Cyc+Mt case, (b) Cyc-Flat case, and (c) over 20–30 h for the Shear case. Terms, as defined in (3), are $(\partial/\partial t)\overline{\rho q}^{xyz}$ (green), $\overline{\nabla\cdot\overline{\rho q\mathbf{u}}^{z}}^{xy}$ (red), and $\overline{P}^{xy}$ (blue).

$$\frac{\partial\overline{\rho q}^{z}}{\partial t}+\nabla\cdot\overline{\rho q\mathbf{u}}^{z}+P=0, \tag{2}$$

where $\mathbf{u}$ is the horizontal velocity vector and P is the surface precipitation rate per unit area (kg m^{-2} s^{-1}).

The volume-integrated moisture budget over boxes 2 and 3,

$$\frac{\partial}{\partial t}\overline{\rho q}^{xyz}+\overline{\nabla\cdot\overline{\rho q\mathbf{u}}^{z}}^{xy}+\overline{P}^{xy}=0, \tag{3}$$

is plotted in Fig. 4 as a function of time using hourly resolution output data. From left to right, the terms in (3) represent the rate of change of airborne water within the volume, the horizontal moisture-flux divergence, and the area-integrated surface precipitation, respectively. For notational compactness, we refer to the cross-mountain axis x as the east–west (E–W) coordinate and the along-mountain y axis as north–south (N–S).

Hourly resolution allows the approximation of the terms in the budget to be within a residual that is never greater than 7% of the largest individual term. We were unable to store the voluminous data required to compute the budget at finer-time resolution, but as a test, we did save data every 2 min over a 2-h period. Using this finer-time resolution data, which is particularly helpful for the evaluation of the time derivative, the magnitude of the residual dropped to 0.4% of the largest individual term, suggesting that the biggest contribution to the residual in Fig. 4 comes from the approximation of the time derivative.

In the Cyc+Mt case (Fig. 4a), the dominant balance is between horizontal moisture-flux convergence (MFC, corresponding to the negative values of $\overline{\nabla\cdot\overline{\rho q\mathbf{u}}^{z}}^{xy}$) and precipitation. There is also a small tendency for the total water in the volume to increase with time. A similar rate of increase in the windward-slope total water occurs in the Cyc-Flat simulation (Fig. 4b). In both cases, this increase is produced by an increase in the moisture accompanying the advance of the warm sector into the region. There is negligible precipitation in the Cyc-Flat case before the approach of the cold front around hour 97, and the horizontal MFC, which balances the increase in the volume-integrated moisture, is dramatically smaller than in the Cyc+Mtn case. In the Shear case, the dominant balance after hour 23 is between precipitation and horizontal MFC. Prior to hour 23, the MFC is balanced by both precipitation and increases in the volume-integrated airborne water. The changes in volume-integrated water in the first 3 h after completing the 20-h ramp-up of the velocity field (i.e., before hour 23) are produced by slowly propagating initial transients.

The dominant balance between horizontal MFC and precipitation also holds when these quantities are averaged parallel to the ridge crest, time averaged, and plotted as a function of distance perpendicular to the crest. Figure 5 shows these y- and t-averaged budget terms from (3):

$$\frac{1}{L_yT}\frac{\partial\overline{\rho q}^{yzt}}{\partial t},\quad \frac{1}{L_yT}\overline{\nabla\cdot\overline{\rho q\mathbf{u}}^{z}}^{yt},\quad \frac{1}{L_yT}\overline{P}^{yt}, \tag{4}$$

as well as the residual, plotted as a function of cross-mountain coordinate x. For the Cyc+Mtn and Cyc-Flat cases, the time averaging interval is $T = 10$ h between 85 and 95 h, while $T = 10$ h between 20 and 30 h in the Shear simulation. In all cases, $L_y = 200$ km and the average is taken over the north–south extent of boxes 2 and 3.

At all points along the cross-ridge transect on the upstream slope, the balance between the horizontal MFC and precipitation is apparent, with precipitation and convergence being clearly strongest in the Cyc+Mtn case and essentially nonexistent in the Cyc-Flat simulation. Also of note is that the extremum in the MFC and precipitation occurs around $x = 860$ km, near the center of the upstream slope in the Cyc+Mtn case, whereas it is closer to the crest at about $x = 885$ km in the Shear case.

b. *Dominance of the east–west moisture-flux convergence*

Given the very tight relation between precipitation and horizontal MFC evident in Figs. 4 and 5, we can isolate dynamical processes responsible for the substantial differences in precipitation between the Cyc+Mtn and Shear cases by further decomposing the contributions to the MFC. The north–south (N–S) and east–west (E–W) contributions of the volume-integrated MFC, $-\overline{\nabla\cdot\overline{\rho q\mathbf{u}}^{z}}^{xy}$, are plotted as a function of time in Fig. 6. Note that having switched our focus to convergence, rather than the full moisture budget, we plot the negative of the second term in (3), so that convergence is now positive.

Figure 6 shows the total MFC is dominated by the E–W contribution in both simulations. During the warm-sector period from 85 to 95 h, the E–W convergence is more than twice as strong in the Cyc+Mtn case as in the Shear case. The N–S moisture fluxes are weakly convergent in the Cyc+Mtn case and weakly divergent in the Shear simulation. This contrast in the N–S moisture-flux convergence does tend to produce higher rain rates in the Cyc+Mtn case, but most of

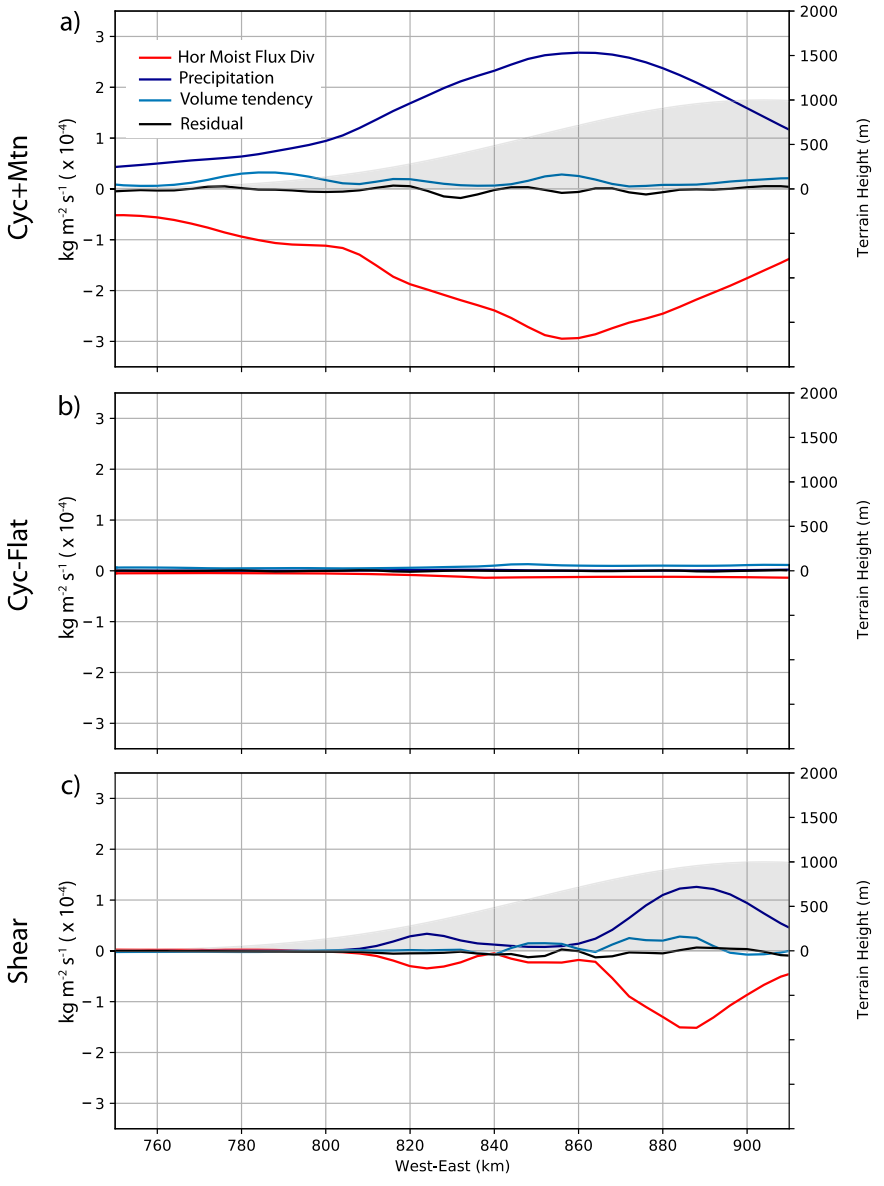

FIG. 5. Contributions of the y-, z-, and t-averaged moisture budget as detailed in (4) plotted as a function of cross-ridge coordinate. Also shown is the mountain profile as gray shading: (a) Mtn+Cyc, (b) Cyc-Flat, and (c) Shear cases.

the difference in precipitation arises from the behavior of the E–W moisture fluxes. The volume-integrated E–W flux divergence can be further decomposed as

$$-\overline{\frac{\partial}{\partial x}(\overline{\rho q u}^{z})}^{xy} = -\overline{u\frac{\partial \rho q}{\partial x}}^{xyz} - \overline{\rho q\frac{\partial u}{\partial x}}^{xyz}. \tag{5}$$

The first term on the right-hand side of (5), which we refer to as the moisture advection, represents the only type of MFC included in simple upslope precipitation models, which neglect the variation in u along the windward slope and give negative values of $\partial\rho q/\partial x$ as the flow ascends the slope and hydrometeors precipitate out. The second term, the velocity convergence, reflects the influence of changes in the wind speed as the flow ascends the slope. These two terms are plotted, along with their sum, in Fig. 7.[2] The moisture advection term is positive

[2] While the left-hand side of (5) can be easily evaluated as the difference between the fluxes at the upstream and downstream faces of the control volume, the terms on the right-hand side need to be integrated across the interior of the volume. Here, we approximate the derivatives with respect to x at constant z, by the derivatives along a coordinate surface. This approximation leads to roughly 10% error in the total MFC, as suggested by a comparison of the left-hand side of (5) plotted as the blue lines in Fig. 6 with the right-hand side of (5) plotted as the black lines in Fig. 7.

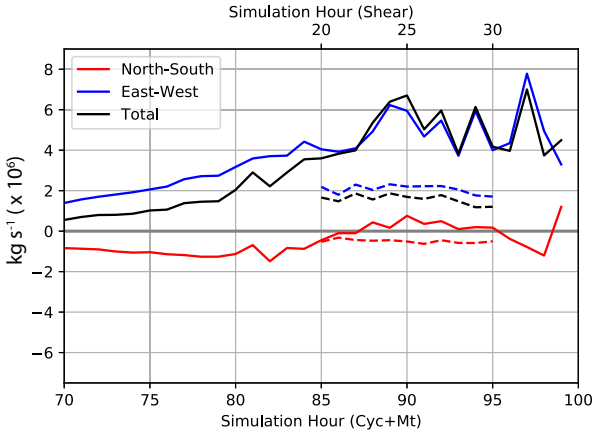

FIG. 6. Decomposition of the volume-integrated MFC over boxes 2 and 3 into N–S (red) and E–W (blue) contributions, along with their sum (black), plotted as a function of time: Cyc+Mtn (solid) and Shear (dashed).

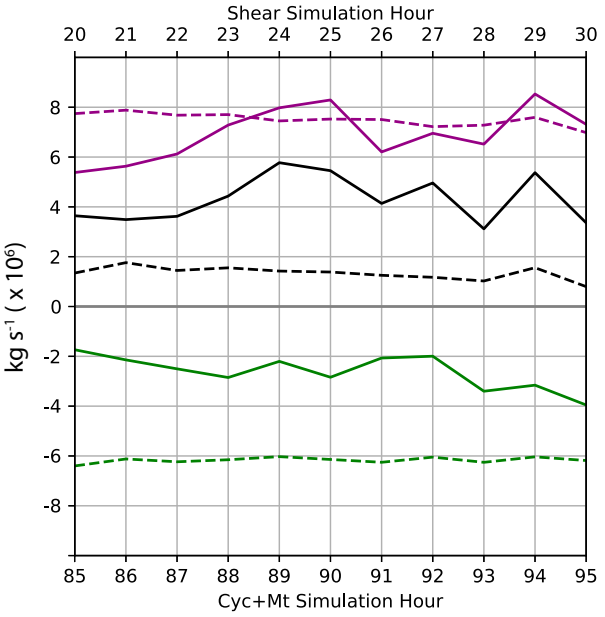

FIG. 7. Contributions to the volume-integrated E–W horizontal MFC plotted as a function of time for the Cyc+Mtn case (solid) and the Shear simulation (dashed): moisture advection (purple), velocity convergence (green), and their sum (black).

and has a similar magnitude, ranging between 6×10^6 and 8×10^6 kg s^{-1} throughout most of the period in each simulation. In contrast, the velocity convergence term is negative over the same period, and its magnitude in the Shear simulation (-6×10^6 kg s^{-1}) is roughly twice that in the Mtn+Cyc case. As a consequence, the E–W MFC is approximately twice as strong in the Mtn+Cyc case as in the Shear case.

To isolate the processes responsible for this difference, it helps to first examine the vertical distribution of the MFC, which is plotted as a function of distance above ground level (AGL) in Fig. 8 for the Cyc+Mtn, Cyc-Flat, and Shear cases. Consistent with Figs. 4b and 5b, the total horizontal MFC for the Cyc-Flat case is nearly zero; moreover, it is almost zero at every level, and the individual N–S and E–W contributions drop rapidly to zero above 3 km AGL. In the other two cases, significant total MFC values are generated by mountain-induced perturbations through a much deeper layer, up to roughly 6 km AGL.

Both the total and E–W contributions of the horizontal moisture-flux divergence are convergent at all levels in the Cyc+Mtn case, and above 3 km AGL, they have roughly similar values to those in the Shear case. But particularly below 1 km AGL, the differences between the Cyc+Mtn and Shear cases become quite large. In the lowest 1-km-deep layer, there is strong MFC in the E–W contribution in the Cyc+Mtn case, but in contrast, there is almost no net convergence in the Shear case because there is strong divergence below 500 m. In the Mtn+Cyc, but not the Shear, case, there is also strong N–S MFC, although it is largely offset by divergence aloft in the layer $1.5 \leq z \leq 5$ km.

c. *Dynamical processes responsible for the differences in east–west moisture-flux convergence*

Having established that the difference in the E–W MFC between the Cyc+Mtn and Shear cases is dominated by contributions from the lowest couple kilometers and that the gradient in the cross-ridge velocity makes the most significant contribution to those differences, consider the u-velocity cross sections shown in Fig. 9.

These velocities are averaged N–S over box 3, at the center section of the terrain; vertical lines mark the lowest 2 km of the east and west faces of the budget volume. The flow through both sides of the budget volume is faster in the Shear case than in the Cyc+Mtn case, but the velocity difference is greater at the downstream face, creating stronger velocity divergence in the Shear case. This difference in the acceleration across the windward slope is associated with a significant difference in the strength of the lee-wave amplitude in the two cases, with higher amplitude, and stronger downslope flow, in the Shear case.

Yet the upstream sounding in the Shear case almost exactly matches that in the Cyc+Mtn case; why then is the mountain-wave response so different? The difference lies in the artificial startup used in the Shear simulation and is even more extreme in the Shear-No-Ramp case, where instead of gradually ramping up over a 20-h period, the large-scale cross-mountain flow is instantaneously accelerated from rest. Even 22 h after the instantaneous startup, the mountain wave and the windward-slope velocity divergence in the Shear No-Ramp case remain significantly stronger than in the Shear case with the gradual ramp-up, as shown in Fig. 9c. A consequence of the persistence of this stronger mountain wave is that the precipitation in the Shear-No-Ramp case remains distinctly lower than that in the Shear case even 35 h after both simulations are initialized (Fig. 1).

The artificial cross-mountain initialization leads to stronger mountain waves in the Shear and particularly the Shear-No-Ramp cases because there is unrealistic transport of warm

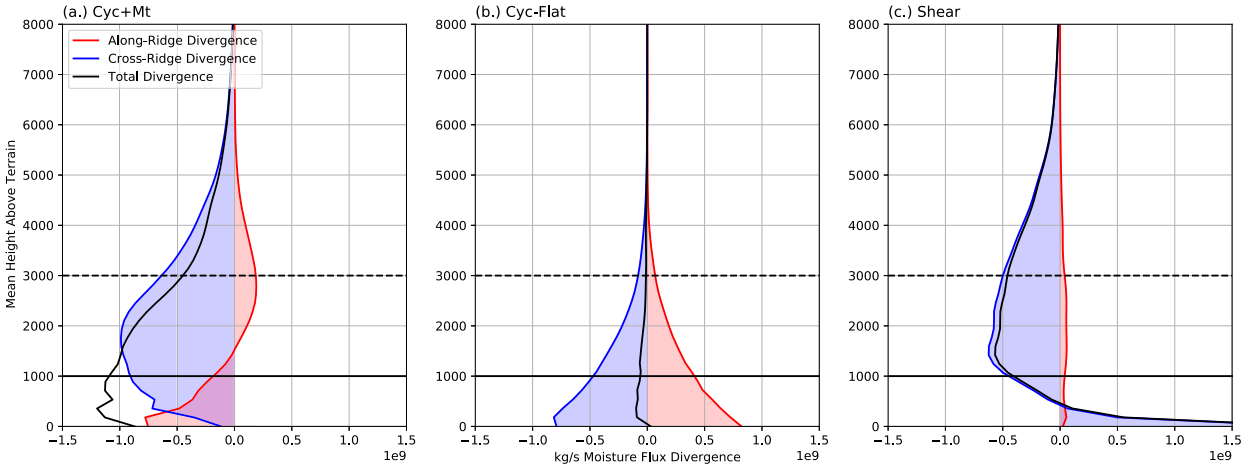

FIG. 8. Horizontal moisture-flux divergence averaged over boxes 2 and 3 as a function of height AGL; N–S (red), E–W (blue), and total (black) for cases (a) Cyc+Mtn and (b) Cyc-Flat averaged over 85–95 h, and (c) Shear averaged over 20–30 h. Horizontal grid lines at $z = 1000$ and 3000 m are emphasized.

mountaintop air into the lee as the cross-mountain flow accelerates. At $t = 0$, the isentropes are horizontal and the warmest potential-temperature air in contact with the ground is at mountaintop. If the flow accelerates rapidly, this warm air is quickly transported into the lee and tends to hydrostatically amplify the developing mountain-wave trough. On the other hand, if the flow accelerates slowly, some of the horizontal temperature (buoyancy) gradient, which would otherwise develop as the high potential-temperature air advects into the lee, is radiated away by gravity waves.

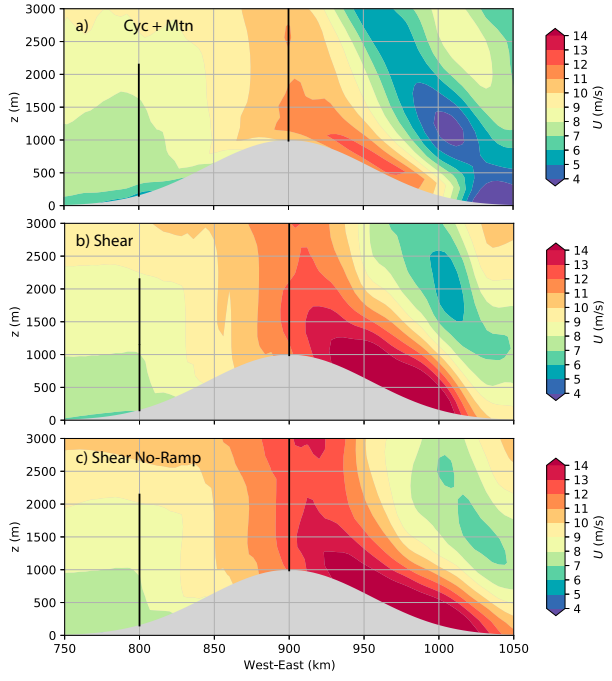

FIG. 9. Contours of u (m s^{-1}) averaged N–S over box 3 for cases (a) Cyc+Mtn at 95 h and (b) Shear and (c) Shear No-Ramp, both at 22 h. Thick vertical lines mark the lowest 2 km of the east and west faces of the budget volumes used in the MFC budget computations.

In Fig. 10, trajectories in low-level flow across the crest from the Shear and Shear-No-Ramp initialization are compared with those during a period of cross-mountain flow acceleration in the Mtn+Cyc simulation. The cross-mountain winds at 81 h in the Cyc+Mtn simulation are similar to those in the Shear case at 9 h, so these times are selected to begin the Mtn+Cyc trajectory (Fig. 10a) and the trajectory in the Shear simulation (Fig. 10b).

The trajectories are computed using N-S averaged velocities over boxes 2 and 3, with points showing the x–z air parcel location every hour. Also shown are isentropes of the potential-temperature field, averaged over the same spatial domain and over the last hour of the trajectory. These are nonsteady diabatic flows (with some clouds developing shortly after the startup), so the isentropes do not approximate trajectories. The downstream translation of air parcels is very similar for the first 2 h in Figs. 10a and 10b, after which time the stronger mountain wave in the Shear case produces greater downstream parcel displacements. While the mountain wave, evident in the potential-temperature field, is stronger in the Shear case than in the Mtn+Cyc simulation, it is strongest in the Shear-No-Ramp case (Fig. 10c).

The trajectories in Figs. 10b and 10c cover time periods over which downstream transport by the horizontal large-scale flow is identical in each simulation. Appropriate times for comparing air parcel locations in the Shear and Shear-No-Ramp cases were computed as follows. Over a time t_{nr} in the Shear-No-Ramp case, environmental winds would carry a parcel downstream an x-coordinate distance $U(z)t_{nr}$, where $U(z)$ is the x-component of the flow in the sounding extracted from large-scale environment upstream of the mountain as discussed in LT1. In the Shear case, the wind speed increases linearly with time over 20 h, and at time t_r after startup, a parcel would translate over a distance $U(z)t_r^2/40$. Equating these

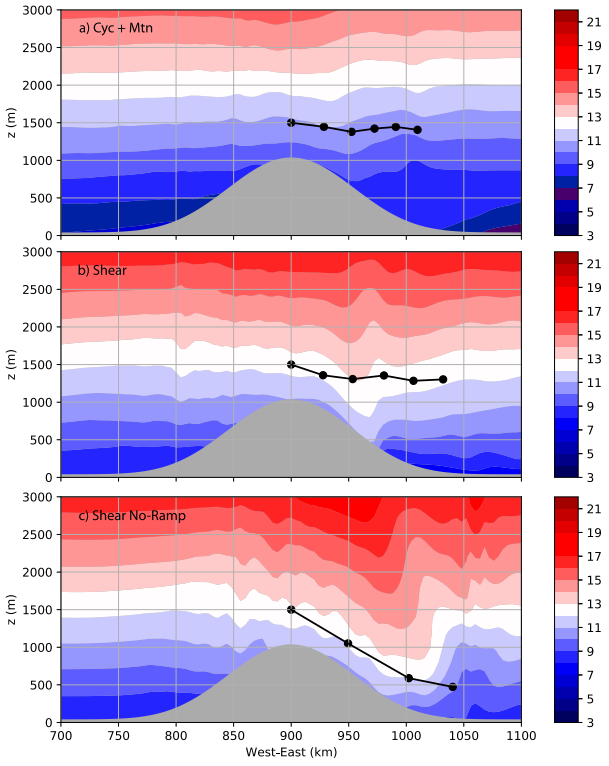

FIG. 10. Cross-mountain trajectories, computed from north–south averaged velocities over boxes 2 and 3 for cases (a) Mtn+Cyc over 81–86 h, (b) Shear over 9–14 h, and (c) Shear No-Ramp over 2–5 h (black curves with points showing location every hour). Also plotted are contours of north–south averaged potential temperature (color fill; °C) time-averaged over the last hour of each trajectory. Each trajectory begins over the ridge crest at $z = 1.5$ km.

expressions, parcels in the Shear case at time t_r would occupy the same positions as those in the Shear-No-Ramp case provided

$$t_r = (40t_{\mathrm{nr}})^{1/2}, \tag{6}$$

where the time units are hours. Figure 10b shows the trajectories in the Shear case over the period 9–14 h, and using (6) to match endpoints, Fig. 10c shows the 2–5-h trajectory for the Shear-No-Ramp case. Although the trajectories are computed using the actual N–S averaged velocities, not simply the background flow, the downstream translation over each period is about the same. Since the winds over this period are weaker in the Shear case, it takes 5 h for a parcel to cover about the same distance it moves in 3 h in the Shear-No-Ramp case. The stronger lee-wave response in the Shear-No-Ramp case is associated with much greater air parcel descent, as well as a much more pronounced trough in the θ field. Comparing the panels in Fig. 10, it is apparent neither the 20-h-ramp-up nor the no-ramp-up initialization yield simulations that satisfactorily approximate the mountain-wave development in the Cyc+Mtn case.

Although the upstream static stability, which is the important thermodynamic variable for classical dry mountain-wave dynamics, is the same in all three cases, the potential temperatures plotted in Fig. 10 for the Mtn+Cyc case are colder than those in the other panels because the sounding for the Shear and No-Ramp Shear cases was taken at hour 96 of the Cyc-Flat simulation when the air in the warm sector had become warmer than that averaged over the final hour of the Cyc+Mtn trajectory (hours 85–86). The warmer approaching environment is evident in Fig. 10a from the gradual upward slope toward the east of all but the lowest-level isentrope. Such advection of warmer air from the south illustrates how, in contrast to the Shear and Shear-No-Ramp cases, the leeside conditions in the Mtn+Cyc case are not solely determined by the flow upstream of the ridge.

4. Seeder–feeder enhancement

An alternative explanation for enhanced orographic precipitation under the influence of a large-scale low pressure system is the seeder–feeder effect, in which ice particles falling from an upper-level cloud seed a low-level feeder cloud where the falling hydrometeors grow rapidly through accretion or collision and coalescence. Seeder–feeder enhancement has been documented to significantly increase rainfall over small hills (Bergeron 1965). It is also active over mountains, although over larger barriers, it can be difficult to disentangle seeder clouds generated by synoptic-scale forcing from upper-level clouds directly forced by orographic ascent (Minder et al. 2008).

In the following, we evaluate the potential of artificially boosted seeder–feeder enhancement to generate precipitation rates comparable to those in our Cyc+Mtn simulation by adding upper-level ice clouds to two additional shear-flow simulations. These simulations are identical to the basic Shear simulation (including the linear 20-h ramp-up of the velocity field) except that an artificial ice cloud is inserted at hour 20 between 5 and 6 km AGL, so that it rises over the terrain and spans the entire north–south length of the ridge. The cloud extends 700 km upstream from the ridge crest, beginning at an initial location of $x = 200$ km on the nested domain. This cloud is held constant in time and space throughout the remainder of the simulation.[3] As ice particles grow and fall out, the ice cloud is not diminished; water mass is not conserved. While not entirely realistic, continually replenishing the cloud ice gives an approximate upper bound on seeder–feeder effects for a given cloud–ice mixing ratio, and such seeding turns out to be inadequate to account for the intensity of the precipitation in the Mtn+Cyc simulation.

East–west cross sections of cloud-ice and cloud-liquid-water concentrations, averaged over 10 h and north–south over boxes 2 and 3, are shown for all simulations in Fig. 11. A thin ice cloud, with concentrations between 0.001 and 0.002 g kg^{-1}, is present throughout the region in the Cyc-Flat case, although no liquid-water cloud develops during this prefrontal period (Figs. 11a,b). The distribution of this cloud in the horizontal is

[3] The gridpoint values of the ice mixing ratio are held fixed throughout the prescribed cloudy region.

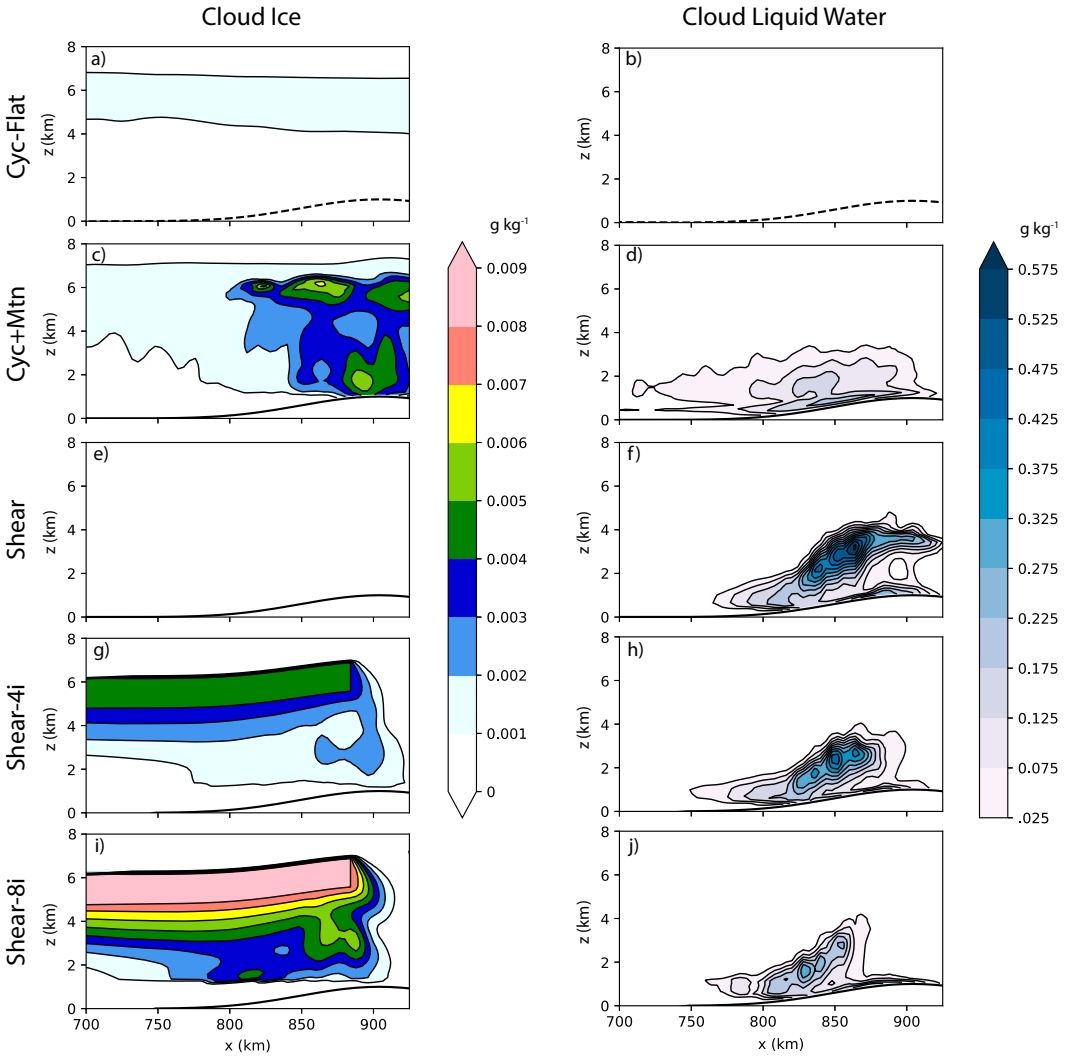

FIG. 11. (left) Cloud ice and (right) cloud-liquid-water mixing ratios (g kg^{-1}) averaged over time and over the north–south extent of boxes 2 and 3 ($700 \leq y \leq 900$ km). Time averages are 85–95 h for the (a),(b) Cyc-Flat; and (c),(d) Cyc+Mtn simulations. Time averages are for 20–30 h of the (e),(f) Shear; (g),(h) Shear-4i; and (i),(j) Shear-8i simulations. Mountain profile is shown by the solid black line and the virtual position of the mountain is shown by the dashed line.

shown by the cloud-top temperature field at 85 h in Fig. 12b. A layer of elevated ice cloud, again with concentrations of 0.001–0.002 g kg^{-1}, is also present at the upstream edge of the plot in the Cyc+Mtn simulation, but in contrast to the Cyc-Flat case, this cloud is thicker at the upstream edge of the plot and its base lowers dramatically as the air ascends the windward slope. The base of the ice cloud extends down to the melting level, whose elevation is approximately the same as the height of the ridge crest. Also in contrast to the Cyc-Flat case, liquid-water cloud is present below about 3 km over the entire windward slope (Figs. 11c,d). The horizontal extent of the Cyc+Mtn cloud tops is shown at 85 h in Fig. 12a.

In contrast to both simulations with a synoptic-scale cyclone, there is no cloud ice above the ridge in the Shear simulation, although a large liquid-water cloud does form as the flow ascends the mountain (Figs. 11e,f). No upper-level cold cloud appears in the horizontal plot of cloud-top temperature field in the Shear case (Fig. 12c).

The ice-cloud and liquid-water-cloud concentrations for the first of the additional seeder–feeder simulations, Shear-4i, are shown in Figs. 11g and 11h. The ice concentration in the fixed seeder cloud is held at 0.004 g kg^{-1}, which is similar to the average cloud-ice concentration in the 5–6-km layer in the Cyc+Mtn case. Sedimentation of this additional ice lowers the cloud base almost as much as in the Cyc+Mtn simulation, although the low-level cloud-ice concentrations are much lower in the Shear-4i case. In comparison with the Shear simulation, the added ice does convert a significant fraction of the liquid-water cloud to falling precipitation, reducing the

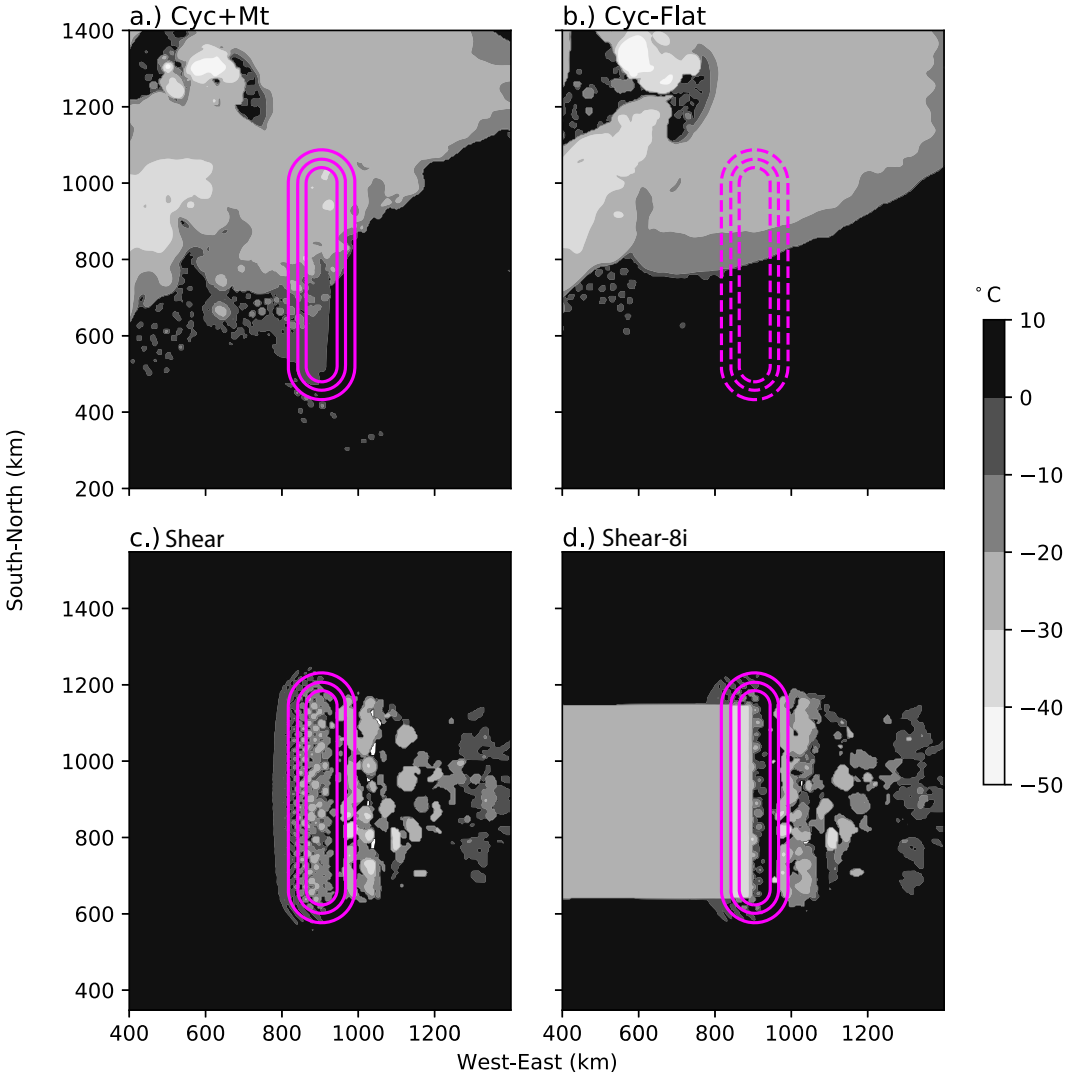

FIG. 12. Cloud top (or clear-air surface) temperatures (°C) at 85 h in the (a) Cyc+Mt and (b) Cyc-Flat simulations; and at 25 h in the (c) Shear and (d) Shear-8i cases. The terrain is contoured in purple every 250 m; the virtual position of the orography in Cyc-Flat is dashed.

concentrations in Fig. 11h compared with those in Fig. 11f. This is also shown quantitatively in Fig. 13, which compares the cloud-liquid-water concentrations for each simulation averaged over 10 h and over the lowest 5 km of boxes 2 and 3. As apparent in Fig. 13, the added ice falling from the seeder cloud significantly reduces the average cloud-liquid-water concentration relative to the Shear simulation, although it is not sufficient to scavenge it down to the 0.06 g kg^{-1} level in the Cyc+Mtn case.

To reduce the cloud-liquid-water concentration over the windward slope to that in Cyc+Mtn simulation, the ice concentration in the fixed upper-level cloud is increased to 0.008 g kg^{-1} in the second additional seeder–feeder shear-flow simulation, Shear-8i. This additional ice significantly thickens the seeder cloud (Figs. 11i and 12d), and the increased seeding further diminishes the cloud-liquid-water concentrations over the windward slope (Figs. 11j). The data plotted in Fig. 13 confirm that the seeding in Shear-8i is sufficiently intense to drop the average cloud-liquid-water concentration over the windward slope below that in the Mtn+Cyc simulation.

How does the extra seeding change the precipitation in these simulations? The precipitation rate, averaged over 10 h and boxes 2 and 3, is plotted in Fig. 14. First, comparing the effects of seeding in the shear-flow simulations, the seeding from the fixed upper-level cloud increases the precipitation rate in the Shear-4i case relative to the basic Shear simulation by more than 50%. On the other hand, the fractional increase in the precipitation rate from the Shear-4i to the Shear-8i case is rather small, and the absolute increase in the rate from the extra ice sedimentation from the Shear-4i to the Shear-8i simulation is only about half that produced in the Shear-4i case relative to the basic Shear simulation.

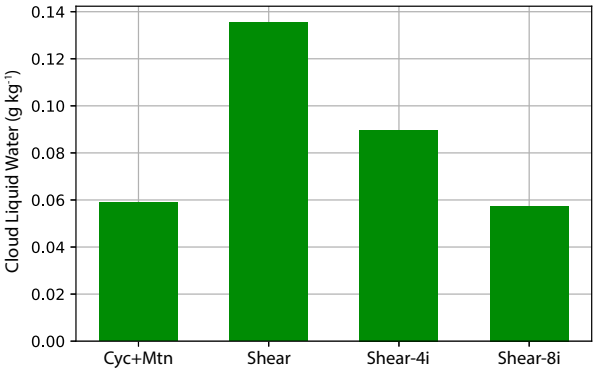

FIG. 13. Cloud-liquid-water concentration (g kg^{-1}) averaged over boxes 2 and 3 and $0 \leq z \leq 5$ AGL between 85 and 95 h for the Cyc+Mt simulation and between 20 and 30 h for the shear-flow simulations.

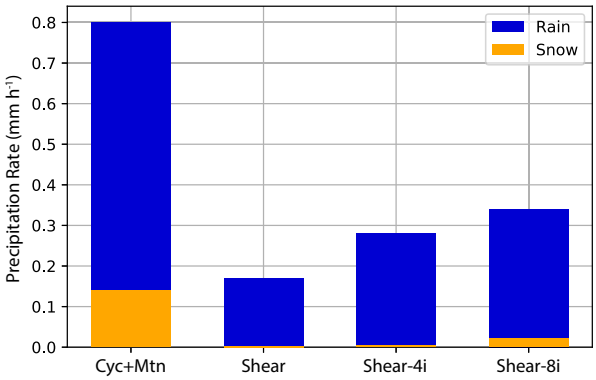

FIG. 14. The mean hourly rate of precipitation rate in boxes 2 and 3 over the windward slope for the Cyc+Mt simulation averaged over 85–95 h and for the three shear-flow simulations averaged over 20–30 h.

Most significantly, the precipitation rate in the Shear-8i case is less than half that in the Cyc+Mtn simulation despite the Shear-8i case having an extra fixed moisture source that provided enough seeding to keep the average liquid-water concentration in the low-level orographic cloud below that in the Cyc+Mtn simulation. These simulations certainly demonstrate that the seeder–feeder mechanism can enhance the simulated orographic precipitation, but they nevertheless also suggest the difference in precipitation rates in the Cyc+Mtn and Shear cases is much too large to attribute to seeder–feeder enhancement.

One might wonder how the different cloud distributions evident in Fig. 11 change the effective moist static stability, and thereby influence the strength of the mountain wave and the precipitation in simulations with shear and added ice cloud. Because the latent heat of fusion for water is less than 1/6 that of the latent heat of vaporization, there is little difference in static stability between air columns with otherwise identical thermodynamic profiles that are either unsaturated or saturated with respect to ice (with additional ice cloud present in the saturated case). To compare the regions with the greatest static stability changes due to saturation, compare the outlines of the liquid-water clouds in Figs. 11f, 11h, and 11j. The largest region of low static stability is actually in the Shear simulation; in contrast, liquid water is removed well before the crest in the Shear-8i simulation. The impact of these changes on the full mountain-wave morphology is complex. Ascent over the windward slopes is modestly weakened by adding the ice cloud, while descent in the leeside trough is stronger, particularly in the Shear-8i case. Therefore, the dynamical changes associated with the enhancement of precipitation through the seeder–feeder mechanism provide a modest negative feedback on the otherwise substantial microphysical enhancement of the precipitation in these runs.

5. Conclusions

In LT1, we showed that idealized process simulations of orographic precipitation forced by horizontally homogeneous environmental winds significantly underpredict the precipitation that would be expected for a given integrated vapor transport (IVT) in real-world observations. LT1 also showed that a similar discrepancy between IVT and precipitation rate could be reproduced in a series of more complex idealized simulations. First, we simulated the interaction of the warm sector of a prototypical midlatitude cyclone with an isolated north–south mountain. Then, a sounding was extracted from the environmental flow upstream of the mountain and used to force a closely related Shear simulation with horizontally uniform environmental winds. Although the thermodynamic, cross-mountain wind profiles, and IVT in the Shear simulation matched those in the full Cyc+Mtn simulation, far more precipitation was produced in the Cyc+Mtn case.

The main difference between the precipitation rates in the Cyc+Mtn and Shear cases was traced to the contrast in cross-mountain (E–W) moisture-flux convergence (MFC) over the windward slopes. The total windward-slope MFC nearly balanced the precipitation, both during the slowly evolving warm-sector passage in the Mtn+Cyc simulation and in the quasi-steady Shear simulation. Recalling the x coordinate is directed toward the east, the E–W MFC can be decomposed as

$$-\frac{\partial}{\partial x}(\rho q u) = -u\frac{\partial \rho q}{\partial x} - \rho q \frac{\partial u}{\partial x}, \tag{7}$$

where the negative signs make the convergence and contributions thereto positive and each term would be vertically integrated through the depth of the flow.

Moisture advection, the first term on the right-hand side in (7), is responsible for all the MFC in simple upslope precipitation models, where the wind speed may even be constant, and condensation and precipitation decrease the total-water mixing ratio as a function of distance up the slope. Yet the discrepancy in the IVT–precipitation rate between the Cyc+Mtn and the Shear simulations arises primarily from the second term involving the convergence of the upslope velocity over the windward slope. As shown in Fig. 9, the winds at the mountain crest are stronger than those at the same height AGL upstream due to the presence of mountain waves, implying that the last

term in (7) promotes divergence and lower precipitation rates. This divergence is stronger in the Shear simulation, which develops stronger mountain waves than those in the Cyc+Mtn case.

The strong mountain wave in the Shear simulation is a consequence of the artificial startup procedure, in which the winds are linearly ramped up over a 20-h period to match the final environmental wind profile. But the gradual ramp-up itself is not the problem, the mountain wave is much stronger in the No-Ramp Shear simulation in which the full-amplitude environmental wind profile is simply initialized throughout the domain. The persistence of effects from the initialization of the Shear and No-Ramp-Shear simulations extends from the end of the initialization at 20 h through the remainder of each run (to 36 h), during which the Shear-case precipitation remains distinctly higher (Fig. 1), and the mountain wave weaker, than in the Shear-No-Ramp simulations.

The key problem with the Shear simulation, and by implication, the other previously cited process-based orographic precipitation studies, is the assumption that the upstream conditions entirely determine the atmosphere's influence on the mountain-wave structure. Even when the flow is slowly evolving, leeside conditions, both at the initial time, and as generated by the large-scale 3D airflow around the orography, also play an important role in regulating atmospheric circulations above the ridge. Mayr and Armi (2008) emphasized the importance of airmass differences in driving the southerly flow of Alpine föhn across the central Alps. Siler and Durran (2016) emphasized the role of cold pools east of the Cascade Mountains of Washington in minimizing lee-wave amplitude in orographic precipitation events with weak rain-shadowing. But in comparison with the south föhn and weak-rain-shadow events, the airmass differences between the windward and leeward sides of the ridge in the Mtn+Cyc case are modest and were zero before the development of the cyclone in the initial large-scale zonally uniform environment. The airmass differences across the orography were likely also modest in the observed orographic rain events over the quasi-circular Olympic Mountains and the coastal mountains of Northern California. The factors regulating the leeside environment in situations like the Cyc+Mtn case would be an interesting topic for future study.

An alternative microphysical process that can also enhance orographic precipitation during the passage of midlatitude cyclones is the seeder–feeder mechanism. If the differences in the precipitation intensity between the Mtn+Cyc and Shear simulations were due to seeder–feeder enhancement, the first term on the right-hand side of (7) should be larger in the Mtn+Cyc case, but this term is approximately equal or even small than that in the Shear simulation (Fig. 7). Nevertheless, we further explored the potential of the seeder–feeder mechanism to enhance the precipitation in our shear-flow simulations by adding an elevated source of ice crystals in the form of a fixed midlevel cloud above the windward slope. Even when ice sedimentation from a very thick artificial seeder cloud was sufficient to scavenge the cloud-liquid-water concentrations over the upstream slope to values below those in the Mtn+Cyc simulation, the accumulated precipitation remained less than half that in the Mtn+Cyc case. Therefore, although we were able to increase orographic precipitation by adding seeder clouds to our Shear simulation, the increase was not nearly large enough to account for the difference between the Shear and the Cyc+Mtn cases.

Our results highlight the difficulty in formulating process studies involving mesoscale atmospheric circulations. Such studies often strive for computational efficiency using a small numerical domain that limits the interactions between the target phenomena and the larger-scale environment. At least in the case of orographic precipitation, this can also limit the realism of the simulation by overemphasizing the importance of the upstream environment and failing to capture all the factors regulating the conditions in the lee of the crest.

Acknowledgments. Our manuscript was substantially improved by the comments from three anonymous reviewers. This research was supported by NSF Grants AGS-1545927 and AGS-1929466. High-performance computing support from Cheyenne (https://doi.org/10.5065/D6RX99HX) was provided by NCAR's Computational and Information Systems Laboratory, sponsored by the National Science Foundation. This work also relied on computational resources at the Extreme Science and Engineering Discovery Environment (XSEDE) which is supported by the National Science Foundation Grant ACI-1548562.

Data availability statement. The output data from our simulations are too large to archive but may be regenerated using the community WRF Model. The technique for initializing idealized *f*-plane baroclinically unstable flows is thoroughly discussed in Lloveras and Durran (2024). The Python code for generating such initial conditions and the instructions for evolving them in WRF are publicly available at https://github.com/lloverasdan/init-bwave. The WRF Model is available at https://www.mmm.ucar.edu/models/wrf.

REFERENCES

Bergeron, T., 1965: On the low-level redistribution of atmospheric water caused by orography. *Suppl. Proc. Int. Conf. Cloud Phys., 1965*, Tokyo, 96–100.

Cannon, D. J., D. J. Kirshbaum, and S. L. Gray, 2012: Under what conditions does embedded convection enhance orographic precipitation? *Quart. J. Roy. Meteor. Soc.*, **138**, 391–406, https://doi.org/10.1002/qj.926.

Colle, B. A., 2004: Sensitivity of orographic precipitation to changing ambient conditions and terrain geometries: An idealized modeling perspective. *J. Atmos. Sci.*, **61**, 588–606, https://doi.org/10.1175/1520-0469(2004)061<0588:SOOPTC>2.0.CO;2.

Houze, R. A., Jr., and Coauthors, 2017: The Olympic Mountains Experiment (OLYMPEX). *Bull. Amer. Meteor. Soc.*, **98**, 2167–2188, https://doi.org/10.1175/BAMS-D-16-0182.1.

Kingsmill, D. E., P. J. Neiman, and A. B. White, 2016: Microphysics regime impacts on the relationship between orographic rain and orographic forcing in the coastal mountains of northern California. *J. Hydrometeor.*, **17**, 2905–2922, https://doi.org/10.1175/JHM-D-16-0103.1.

Kirshbaum, D. J., and D. M. Schultz, 2018: Convective cloud bands downwind of mesoscale mountain ridges. *J. Atmos. Sci.*, **75**, 4265–4286, https://doi.org/10.1175/JAS-D-18-0211.1.

Lloveras, D. J., and D. R. Durran, 2024: Improving the representation of moisture and convective instability in baroclinic-wave channel simulations. *Mon. Wea. Rev.*, **152**, 1469–1486, https://doi.org/10.1175/MWR-D-23-0210.1.

Mayr, G. J., and L. Armi, 2008: Föhn as a response to changing upstream and downstream air masses. *Quart. J. Roy. Meteor. Soc.*, **134**, 1357–1369, https://doi.org/10.1002/qj.295.

Minder, J. R., D. R. Durran, G. H. Roe, and A. M. Anders, 2008: The climatology of small-scale orographic precipitation over the Olympic Mountains: Patterns and processes. *Quart. J. Roy. Meteor. Soc.*, **134**, 817–839, https://doi.org/10.1002/qj.258.

Neiman, P. J., A. B. White, F. M. Ralph, D. J. Gottas, and S. I. Gutman, 2009: A water vapour flux tool for precipitation forecasting. *Proc. Inst. Civ. Eng.: Water Manage.*, **162**, 83–94, https://doi.org/10.1680/wama.2009.162.2.83.

Picard, L., and C. Mass, 2017: The sensitivity of orographic precipitation to flow direction: An idealized modeling approach. *J. Hydrometeor.*, **18**, 1673–1688, https://doi.org/10.1175/JHM-D-16-0209.1.

Purnell, D. J., and D. J. Kirshbaum, 2018: Synoptic control over orographic precipitation distributions during the Olympics Mountains Experiment (OLYMPEX). *Mon. Wea. Rev.*, **146**, 1023–1044, https://doi.org/10.1175/MWR-D-17-0267.1.

Siler, N., and D. Durran, 2015: Assessing the impact of the tropopause on mountain waves and orographic precipitation using linear theory and numerical simulations. *J. Atmos. Sci.*, **72**, 803–820, https://doi.org/10.1175/JAS-D-14-0200.1.

——, and ——, 2016: What causes weak orographic rain shadows? Insights from case studies in the cascades and idealized simulations. *J. Atmos. Sci.*, **73**, 4077–4099, https://doi.org/10.1175/JAS-D-15-0371.1.

Tierney, L., and D. Durran, 2024: Underestimates of orographic precipitation in idealized simulations. Part I: Evidence from unidirectional warm-sector environments. *J. Atmos. Sci.*, **81**, 1419–1433, https://doi.org/10.1175/JAS-D-23-0177.1.

Zagrodnik, J. P., L. A. McMurdie, R. A. Houze Jr., and S. Tanelli, 2019: Vertical structure and microphysical characteristics of frontal systems passing over a three-dimensional coastal mountain range. *J. Atmos. Sci.*, **76**, 1521–1546, https://doi.org/10.1175/JAS-D-18-0279.1.